Eur. Phys. J. C (2025) 85:1390
https://doi.org/10.1140/epjc/s10052-025-15121-w

THE EUROPEAN PHYSICAL JOURNAL C

Regular Article - Theoretical Physics

Electromagnetic properties of heavy-light mesons

A. S. Miramontes[1,a], **J. Papavassiliou**[1,b], **J. M. Pawlowski**[2,3,c]

[1] Department of Theoretical Physics and IFIC, University of Valencia and CSIC, 46100 Valencia, Spain
[2] Institut für Theoretische Physik, Universität Heidelberg, Philosophenweg 16, 69120 Heidelberg, Germany
[3] ExtreMe Matter Institute EMMI, GSI, Planckstrasse 1, 64291 Darmstadt, Germany

Received: 9 September 2025 / Accepted: 24 November 2025

Abstract Within the Bethe–Salpeter framework, we present a computation of space-like electromagnetic form factors for pseudoscalar mesons, including light and heavy-light systems. Our approach employs a flavour-dependent variation of the standard Taylor effective charge, which contains key contributions from the quark-gluon vertices. This effective interaction is a common ingredient of all relevant dynamical equations, and accommodates the crucial mass differences between the various quark flavours. Particular attention is paid to the nonperturbative determination of the quark-photon vertex. The computed electromagnetic form factors for the pion and the kaon mesons show excellent agreement with experimental determinations. In addition, the predictions for the charge radii of heavy-light systems are in overall good agreement with lattice QCD.

1 Introduction

The electromagnetic form factors (EFFs) of light mesons, in particular those of the pion and the kaon, are of key importance for the understanding of the internal structure and dynamics of hadrons in terms of their quark and gluon constituents. Over the past decades, both experimental measurements and theoretical investigations have made significant progress in exploring these form factors across various momentum-transfer regimes.

From the theoretical point of view, hadronic form factors have been extensively studied within the framework of the Bethe–Salpeter equations (BSEs), a covariant approach for describing bound states in quantum field theory [1–6]. This framework has been adopted in numerous studies of the EFFs of light mesons [7–22] and spectroscopy [23–33], achieving progressively higher levels of precision and sophistication. On the lattice QCD side, a plethora of calculations is available for light mesons [34–40].

On the experimental side, the precise determination of the pion and kaon EFFs remains a priority for contemporary and future hadronic physics programs. Upcoming experiments at major facilities, such as Jefferson Lab [41], the U.S. Electron-Ion Collider (EIC) [42], and the Electron-Ion Collider in China (EicC) [43], are expected to provide accurate data on light meson form factors, particularly in the high-Q^2 region.

Within the BSEs formalism, EFFs are calculated using the so-called "impulse approximation", where the interaction of the photon with the quark-antiquark system is mediated via the dressed quark-photon vertex and the Bethe–Salpeter (BS) amplitude of the meson. An important ingredient of this calculation is the quark-photon vertex itself, which we compute here using its full general structure. In particular, we include both the longitudinal components satisfying the Ward-Takahashi identity (WTI) for electromagnetic current conservation, as well as the transverse components that capture dynamical effects beyond the bare vertex. This comprehensive treatment is essential for the accurate description of the EFFs, particularly in heavy-light systems, where flavour asymmetries can enhance the impact of transverse contributions.

While the light sector has been thoroughly analyzed [7–20,22,44], the inclusion of heavy-light systems, such as the D, B, and their strange counterparts (D_s, B_s), presents unique challenges, including the treatment of asymmetric quark masses and singularities in the quark propagators.

In this work, we employ the BSEs formalism to compute the EFFs of both light and heavy-light pseudoscalar mesons.

[a] e-mail: angel.s.miramontes@uv.es (corresponding author)
[b] e-mail: joannis.papavassiliou@uv.es
[c] e-mail: j.pawlowski@thphys.uni-heidelberg.de

Published online: 06 December 2025

To account for the nontrivial flavour dynamics in these systems, we implement the flavour-dependent interaction previously developed in [32]. In this approach, the interaction strength acquires a natural dependence on the quark flavour via the dynamically generated quark wave function. By incorporating this flavour sensitivity directly into the BSE and gap equation, we can investigate how mass differences between the constituent quarks influence the momentum dependence of the EFF.

It is important to highlight the main differences between the present work and two recent related publications, namely [19] and [45]. In broad terms, the key distinction between these works lies in the composition of the respective interaction kernels employed in the computation of the EFFs. In our case, the renormalization-group invariant interaction kernel is derived by combining the gluon propagator with appropriate dressings of the quark-gluon vertices, which give rise to a modified version of the standard Taylor coupling [32]. Thus, the elements comprising the kernel are obtained from lattice QCD and functional studies, and are, in that sense, rooted in QCD dynamics. In contrast, Ref. [19] employs a weighted version of the rainbow–ladder truncation with the Qin–Chang model [46], where different parameters are chosen for light and heavy mesons, and are subsequently averaged in order to induce the desired flavour-dependence. Instead, in our formulation the flavour-dependence arises naturally from the genuine dressing of the quark-gluon vertices, without introducing separate parameter sets for different quark sectors. Finally, a common drawback of both [19] and [32] is that the dressing of the vertices induces a mild breaking of the axial WTI, see discussion in Sect. 3. Turning to [45], it is based on a light-front quark model [47,48], where the wave functions of the mesons are not obtained dynamically, but are rather postulated to be of the Gaussian type, containing a set of parameters that are fitted from experiment. Thus, while the results are in general comparable (see Sect. 5) the theoretical foundation of [45] is quite distinct, relying on additional phenomenological inputs and adjustable parameters not needed in our approach, or that of [19].

The article is organized as follows. In Sect. 2 we present the general framework that will be employed throughout this work. In Sect. 3 we present a quantitative study of the amount of symmetry violation stemming from the use of the flavour-dependent interaction in the quark gap equation. In Sect. 4 we carry out a detailed analysis of the quark-photon vertex, and present results for all of its form factors. Section 5 contains the main results of this work, namely the EFFs and charge radii, together with an extensive comparison with experiment, lattice QCD, and a variety of approaches. In addition, we present a detailed error analysis, which confirms the robustness of our results under variations of the main inputs. Finally, in Sect. 6 we discuss our conclusions.

2 General framework

In this section we review the standard framework employed for the computation of the EFFs, and discuss the key dynamical equations and their main ingredients.

2.1 Electromagnetic form factors in the impulse approximation

Mesonic form factors are extracted from the physical amplitude that describes the interaction between a meson and an electromagnetic current, $j_\mu(x) = \overline{\psi}(x)\gamma_\mu\psi(x)$. In the BSEs framework, the current is calculated by means of the coupling of an external photon to each of the constituents of the bound state. The corresponding hadronic matrix element is given by $J_\mu(p_{\rm av}, q) = \langle \mathbf{s}(p_f)|j_\mu|\mathbf{s}(p_i)\rangle$, where $\mathbf{s}(p_{\rm av})$ denotes the meson under consideration. This matrix element is related to the electromagnetic form factor $F_\mathbf{s}$ of the meson through the expression

$$J^\mu(p_{\rm av}, q) = 2p_{\rm av}^\mu\, F_\mathbf{s}(q^2) \;\longrightarrow\; F_\mathbf{s}(q^2) = \frac{J\cdot p_{\rm av}}{2p_{\rm av}^2}, \tag{2.1}$$

where $p_{\rm av} = (p_f + p_i)/2$ is the total momentum of the meson, p_i and p_f denote the initial and final meson momentum, respectively, and $q = p_f - p_i$ is the photon momentum.

In the impulse approximation [23,49], the conserved current $J^\mu(p_{\rm av}, q)$ describes the coupling of a single photon to a quark-antiquark system, see Fig. 1. The $J^\mu(p_{\rm av}, q)$ is given by the following integral expression

$$J^\mu(p_{\rm av}, q) = \int_k \bar{\mathcal{A}}(k_f, p_f)S(\ell_+)\Gamma^\mu(k_+, q) S(\ell_-)\mathcal{A}(k_i, p_i)S(k_-), \tag{2.2}$$

where $\mathcal{A}$ is the BS amplitude and $\bar{\mathcal{A}}$ its charge conjugated counterpart, Γ^μ represents the quark-photon vertex, and S stands for the quark propagator. The integral measure is denoted by

$$\int_k := (2\pi)^{-4}\int_{-\infty}^{+\infty} \mathrm{d}^4k\,, \tag{2.3}$$

where the use of a symmetry-preserving regularization scheme is implicitly assumed. In addition, the relevant kinematic variables are defined as

$$k_+ = k + \eta p_{\rm av}\,, \quad k_- = k - (1-\eta)p_{\rm av}, \quad \ell_+ = k_+ + \frac{q}{2}, \quad \ell_- = k_+ - \frac{q}{2}\,, \quad s_+ = k_- + \frac{q}{2}, \quad s_- = k_- - \frac{q}{2}\,. \tag{2.4}$$

Here, the parameter η determines the distribution of the total momentum $p_{\rm av}$ between the quark and antiquark. Depending on the quark mass composition, a suitable choice of the value of η leads to a tighter control of the singularities in the quark

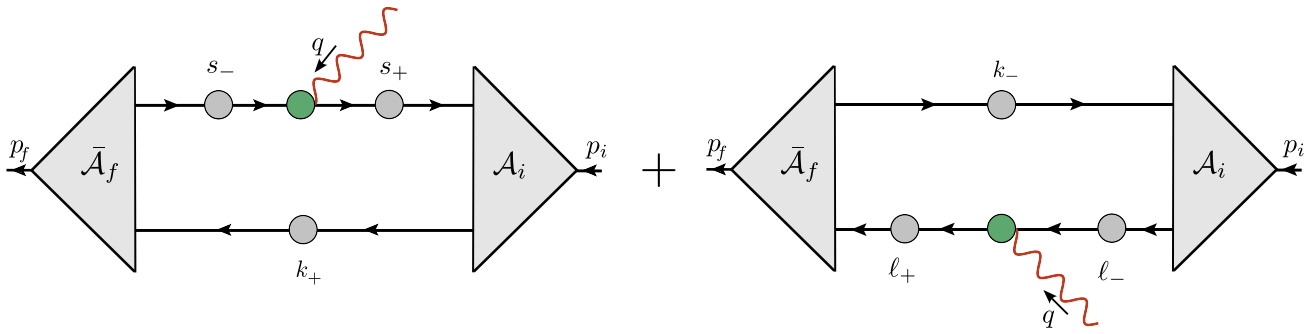

Fig. 1 Diagrammatic representation of electromagnetic current in the impulse approximation, employed for the calculation of electromagnetic form factor. The green and gray circles denote the fully-dressed quark-photon vertex and quark propagator, respectively, and the various kinematic variables are defined in (2.4)

propagator. This, in turn, enhances the numerical stability of the calculation, especially for systems with significant mass disparity, such as heavy-light mesons.

The processes under consideration are elastic, having the same initial and final states, whose common bound state mass is denoted by M. Thus, the on-shell momenta satisfy $p_i^2 = p_f^2 = -M^2$, and $p_{\rm av}$ may be parametrized as $p_{\rm av} = (0, 0, 0, i\sqrt{M^2 + q^2/4})$.

It is important to note that (2.2) accounts for the case where the photon interacts with only one of the valence quarks of the meson; evidently, the contribution of the interaction of the photon with the other quark must be duly added, as shown in Fig. 1. Thus, the complete electromagnetic form factor for a pseudoscalar particle reads,

$$F_{\rm s}(q^2) = e_q F_q(q^2) + e_{\bar{q}} F_{\bar{q}}(q^2), \tag{2.5}$$

where e_q and $e_{\bar{q}}$ are the corresponding electric charges for the quark and antiquark.

2.2 Dynamical equations

The elements comprising (2.2), namely S, $\mathcal{A}$, and Γ^μ are determined from their own dynamical equations, evaluated within appropriately constructed truncation schemes. Recently, a new framework for the study of heavy-light mesons has been put forth [32], where the standard one-gluon exchange interaction is complemented by flavour-dependent contributions stemming from the adjacent quark-gluon vertices (blue circles in Fig. 2). In this treatment, only the classical form factor of each quark-gluon vertex is retained, and is evaluated in the so-called "symmetric" configuration. The Slavnov–Taylor identity satisfied by the quark-gluon vertex links this form factor to the quark wave-function, $A_f(q^2)$, see (2.9), which encodes the flavour-dependence. Specifically, the resulting effective interaction, $\mathcal{I}_{ff'}(q^2)$, is given by

$$\mathcal{I}_{ff'}(q^2) = \tilde{\alpha}_T(q^2) A_f(q^2) A_{f'}(q^2), \tag{2.6}$$

where the effective charge $\tilde{\alpha}_T(q^2)$ is the so-called "modified Taylor coupling", introduced in [32], and shown in Fig. 3. The key difference between $\tilde{\alpha}_T(q^2)$ and the standard Taylor coupling, $\alpha_T(q^2)$, is the inclusion of certain process-independent contributions extracted from the quark-gluon vertex. We stress that the determination of both $\alpha_T(q^2)$ and $\tilde{\alpha}_T(q^2)$ contains *no* adjustable parameters.

The effective interaction of (2.6) is a common ingredient of the three main dynamical equations, namely (2.10), (2.11) and (2.13); in fact, in all of them, it appears in the unique combination

$$D^{\mu\nu}_{ff'}(k) := 4\pi \Delta_0^{\mu\nu}(k) \mathcal{I}_{ff'}(k^2)\,, \tag{2.7}$$

with

$$\Delta_0^{\mu\nu}(k) = \left(\delta^{\mu\nu} - \frac{k^\mu k^\nu}{k^2}\right) \frac{1}{k^2}\,. \tag{2.8}$$

the tree-level gluon propagator in the Landau gauge.

In particular, we have:

(i) The quark propagator, $S_f^{ab}(p) = i\delta^{ab} S_f(p)$, where the index f stands for the quark flavour, taking values $f = u, d, s, c, b$. The standard decomposition of $S_f^{-1}(p)$ is

$$S_f^{-1}(p) = i\not{p}\, A_f(p^2) + B_f(p^2)\,, \tag{2.9}$$

where $A_f(p^2)$ and $B_f(p^2)$ are the dressings of the Dirac vector and scalar tensor structures, respectively. The renormalization-group invariant (RGI) dynamical quark mass, $\mathcal{M}_f(p^2)$, is given by $\mathcal{M}_f(p^2) = B_f(p^2)/A_f(p^2)$. At tree-level, $S_{0,f}^{-1}(p) = i\not{p} + m_f$, where m_f denotes the current quark mass of the flavour f. In addition, the *self-energy*, $\Sigma_f(p^2)$, is defined as $\Sigma_f(p^2) = S_f^{-1}(p) - S_{0,f}^{-1}(p)$.

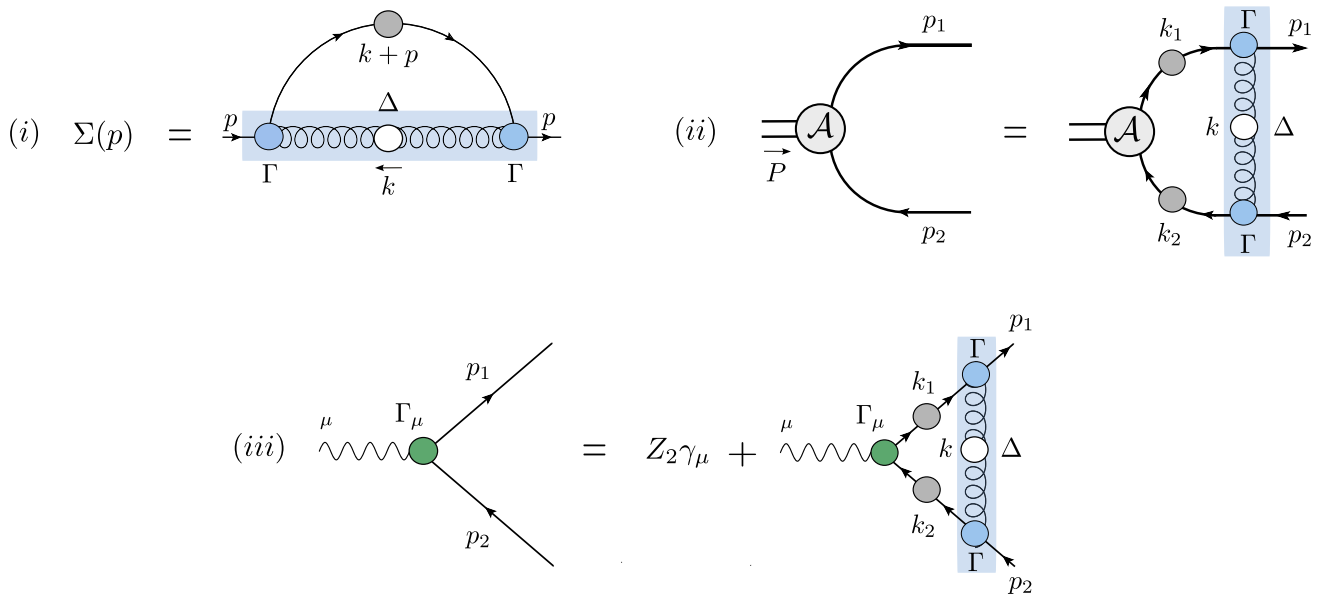

Fig. 2 Diagrammatic representation of the main dynamical components: (i) is the quark self-energy entering in the gap equation; (ii) the BSE for the mesonic wave function; and (iii) the SDE of the quark-photon vertex. Appropriate contributions from the quark-gluon vertices (blue circles) are combined with the scalar factor, $\Delta(k)$, of the Landau-gauge gluon propagator to form the interaction kernel of (2.6), depicted here by the blue band

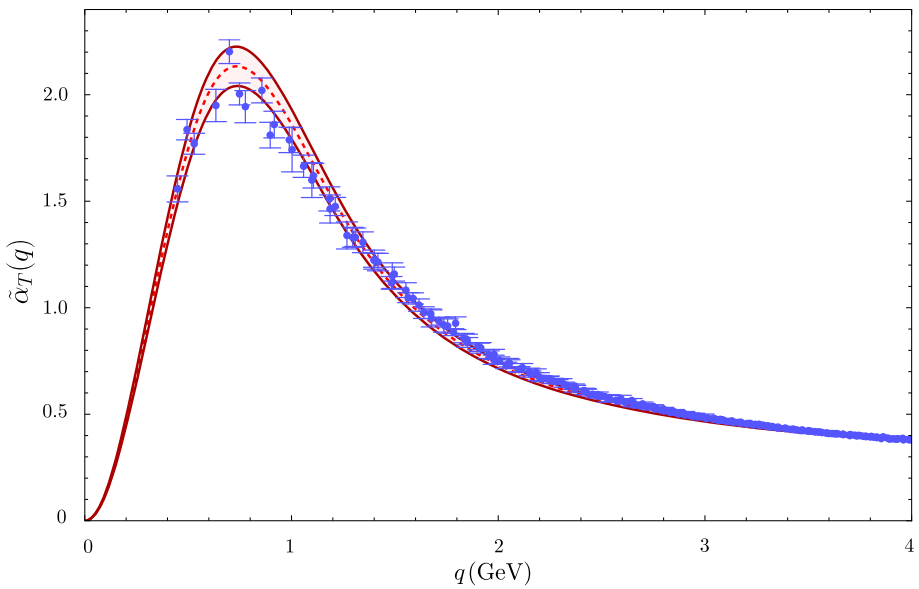

Fig. 3 The modified Taylor effective charge, $\tilde{\alpha}_T(q^2)$, obtained by combining the lattice results of [50] for the standard Taylor coupling, $\alpha_T(q^2)$, with certain propagator-like contributions extracted from the quark-gluon vertices. The dashed curve represents the central parametrization from [32]. The shaded band shows the variation obtained by shifting the fit parameters by one standard deviation ($\pm\sigma$) around their central values, and will be used for the error analysis presented in Sect. 5.3

The evolution of the components $A_f(p^2)$ and $B_f(p^2)$ is determined from the quark gap equation. In terms of the kernel introduced in [32], the renormalized gap equation reads

$$S_f^{-1}(p) = Z_2(i\not{p} + m_R) + \underbrace{C_F \int_k \gamma_\alpha S_f(k+p)\gamma_\beta \, D^{\alpha\beta}_{ff}(k)}_{\Sigma_f(p^2)}\,, \tag{2.10}$$

where $C_F = 4/3$ is the Casimir eigenvalue of the fundamental representation, and m_R is the renormalized current quark mass. The diagrammatic representation of the quark self-energy $\Sigma_f(p^2)$ is shown in Fig. 2, panel (i). Finally, Z_2 is the wave-function renormalization of the quark field, determined within the momentum subtraction (MOM) renormalization scheme [51–54].

(ii) The BS amplitude $\mathcal{A}$ in (2.2) is given by the homogeneous BSE [see panel (ii)] of Fig. 2)

$$\mathcal{A}_{ff'}(p_1, p_2) = -\int_k \gamma_\mu S(k_1)\mathcal{A}_{ff'}(k_1, k_2)S(k_2)\gamma_\nu D^{\mu\nu}_{ff'}(k)\,, \tag{2.11}$$

with $k_i = k + p_i,\ i = 1, 2$.

An alternative parametrization of the momenta, used extensively in the related literature, is given by $P = p_1 - p_2$ and $p = (p_1 + p_2)/2$. In terms of these variables, the tensorial decomposition of the BS amplitude of a pseudoscalar meson is given by

$$\mathcal{A}_{ff'}(p, P) = \Big(\chi_1^{ff'} + i\chi_2^{ff'}\not{P} + i\chi_3^{ff'}\not{p}(p\cdot P) + \chi_4^{ff'}[\not{p}, \not{P}]\Big)\gamma_5\,, \tag{2.12}$$

where the subamplitudes $\chi_i^{ff'} := \chi_i^{ff'}(p, P)$ are functions of the Lorentz scalars P^2, p^2, $p\cdot P$.

(iii) The SDE of the quark-photon vertex, depicted diagrammatically in panel (iii) of Fig. 2, is given by

$$\Gamma_\mu^f(p_1, p_2) = Z_2\gamma_\mu - C_F\int_k \gamma_\alpha S_f(k_1)\Gamma_\mu^f(k_1, k_2)S_f(k_2)\,\gamma_\beta D_{ff}^{\alpha\beta}(k)\,. \tag{2.13}$$

The self-consistent treatment of (2.13) is presented in the next section, where the momentum-dependence of the twelve form-factors comprising $\Gamma_\mu^f(p_1, p_2)$ will be determined.

3 Axial Ward–Takahashi identity and the effective kernel

The dressing of the quark-gluon vertices described in the previous section endows the effective interaction with the required flavour-dependence. However, when the resulting equations are truncated at their lowest order (first term in the skeleton expansion), a violation of the axial WTI occurs for unequal current quark masses. In that sense, the resulting deviations from the exact WTI relations may be interpreted as part of the systematic error of the given method [32]. In this section we demonstrate in detail how this violation comes about, and introduce a procedure for estimating its numerical impact on certain key quantities.

Of central importance for the dynamical chiral symmetry breaking are the axial-vector current, $j^a_{5\mu}(x)$, and the axial current, $j^a_5(x)$, see, e.g., [55] (Ch.11), and [56]. In terms of the fundamental quark fields, $q(x)$ and $\bar{q}(x)$, they are defined as $j^a_{5\mu}(x) = \bar{q}(x)\gamma_5\frac{\lambda^a}{2}\gamma_\mu q(x)$ and $j^a_5(x) = \bar{q}(x)\gamma_5\frac{\lambda^a}{2}q(x)$, where λ^a are the Gell-Mann matrices. Then, the axial-vector vertex, $\Gamma^a_{5\mu}(p_1, p_2)$, and the axial vertex, $\Gamma^a_5(p_1, p_2)$, are defined as the momentum-space transforms of $\langle 0|T[j^a_{5\mu}(0)q(x)\bar{q}(y)]|0\rangle$ and $\langle 0|T[j^a_5(0)q(x)\bar{q}(y)]|0\rangle$, respectively, where T denotes the standard time-ordering operator.

We next suppress the "isospin" indices, and introduce quark flavour indices, f and f'. Then, it is well-known that the axial-vector vertex $\Gamma^{ff'}_{5\mu}(p_1, p_2)$ satisfies the WTI [55,56]

$$P^\mu\Gamma^{ff'}_{5\mu}(p_1, p_2) = S_f^{-1}(p_1)i\gamma_5 + i\gamma_5 S_{f'}^{-1}(p_2) - i(m_f + m_{f'})\Gamma_5^{ff'}(p_1, p_2)\,, \tag{3.1}$$

where $P = p_1 - p_2$.

Within the framework of [32], the vertices $\Gamma^{ff'}_{5\mu}(p_1, p_2)$ and $\Gamma_5^{ff'}(p_1, p_2)$ satisfy the SDEs shown in Fig. 4, namely

$$\Gamma^{ff'}_{5\mu}(p_1, p_2) = \gamma_5\gamma_\mu \underbrace{-\int_k \gamma_\alpha S_{f'}(k_1)\Gamma^{ff'}_{5\mu}(k_1, k_2)S_f(k_2)\,\gamma_\beta D^{\alpha\beta}_{ff'}(k)}_{G^{ff'}_{5\mu}(p_1,p_2)}\,, \tag{3.2}$$

and

$$\Gamma_5^{ff'}(p_1, p_2) = \gamma_5 \underbrace{-\int_k \gamma_\alpha S_{f'}(k_1)\Gamma_5^{ff'}(k_1, k_2)S_f(k_2)\,\gamma_\beta D^{\alpha\beta}_{ff'}(k)}_{G_5^{ff'}(p_1,p_2)}\,, \tag{3.3}$$

where, for latter convenience, we use the short-hand notation $G^{ff'}_{5\mu}(p_1, p_2)$ and $G_5^{ff'}(p_1, p_2)$ to denote the non-trivial parts of the corresponding SDEs.

Evidently, upon contraction with P^μ, the tree-level term $\gamma_5\gamma_\mu$ yields

$$P^\mu\gamma_5\gamma_\mu = S^{-1}_{0,f}(p_1)i\gamma_5 + i\gamma_5 S^{-1}_{0,f'}(p) - 2i(m_f + m_{f'})\Gamma^{ff'}_{0,5}(p_1, p_2)\,, \tag{3.4}$$

where we have used that, at tree-level, $\Gamma^{ff'}_{0,5}(p_1, p_2) = \gamma_5$.

Turning to the quantum part of the calculation, one may directly confirm that, in the case of equal flavours, $f = f'$, the use of the kernel $I_{ff}(q^2)$ in (3.2) and (3.3) preserves the validity of (3.1). In particular, the contraction of $\Gamma^{ff'}_{5\mu}(k_1, k_2)$ by P^μ triggers the WTI of (3.1) under the integral sign of $G^{ff}_{5\mu}(p_1, p_2)$, and one gets

$$\begin{aligned}
P^\mu G^{ff}_{5\mu}(p_1, p_2) &= -i\int_k \gamma_\alpha S_f(k_1)[S_f^{-1}(k_1)\gamma_5 + \gamma_5 S_f^{-1}(k_2) - 2m_f\Gamma_5^{ff}(k_1, k_2)]S_f(k_2)\,\gamma_\beta D^{\alpha\beta}_{ff}(k)\\
&= i\gamma_5\int_k \gamma_\alpha S_f(k_2)\,\gamma_\beta D^{\alpha\beta}_{ff}(k) + i\int_k \gamma_\alpha S_f(k_1)\gamma_\beta D^{\alpha\beta}_{ff}(k)\gamma_5 + 2im_f\int_k \gamma_\alpha S_{f'}(k_1)\Gamma_5^{ff'}(k_1, k_2)S_f(k_2)\,\gamma_\beta D^{\alpha\beta}_{ff}(k)\,,\\
&= \Sigma_f(p_1)i\gamma_5 + i\gamma_5\Sigma_f(p_2) - 2im_f G_5^{ff}(p_1, p_2)\,.
\end{aligned} \tag{3.5}$$

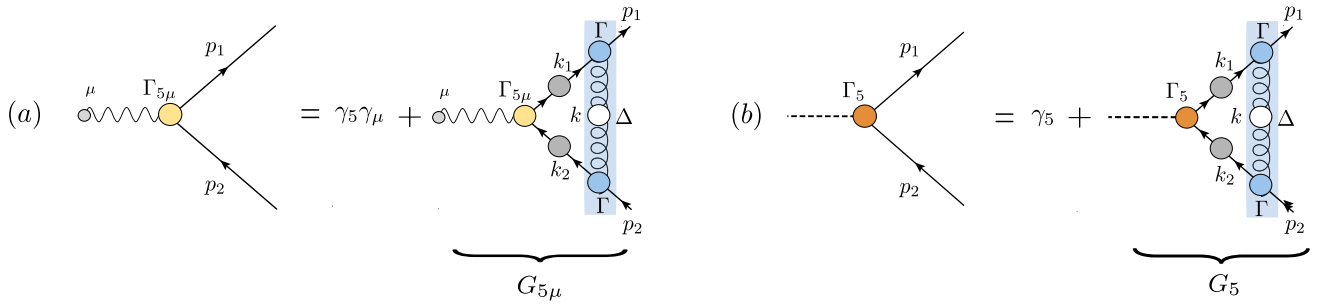

Fig. 4 Diagrammatic representation of the SDE governing the vertex $\Gamma^{ff'}_{5\mu}(p_1, p_2)$ (**a**), and of the SDE governing the vertex $\Gamma^{ff'}_{5}(p_1, p_2)$ (**b**). The wavy line with a small gray circle at its end denotes the axial-vector current $j^a_{5\mu}(x)$, while the dotted line indicates the axial current $j^a_5(x)$. As in the case of Fig. 2, the interaction kernel (blue band) is given by (2.6)

Then, the sum of (3.4) and (3.5) yields precisely the two sides of (3.1), with $f = f'$.

Instead, when $f \neq f'$, the use of the kernel $I_{ff'}(q^2)$ leads to a violation of (3.1). In particular, the repetition of the steps leading to (3.5) now yields

$$P^\mu G^{ff'}_{5\mu}(p_1, p_2) = \widetilde{\Sigma}_f(p_1) i\gamma_5 + i\gamma_5 \widetilde{\Sigma}_{f'}(p_2) - i(m_f + m_{f'}) G^{ff'}_5(p_1, p_2)\,, \tag{3.6}$$

where

$$\widetilde{\Sigma}_f(p_1) = C_F \int_k \gamma_\mu S_f(k_1) \gamma_\nu D^{\mu\nu}_{ff'}(k)\,,$$
$$\widetilde{\Sigma}_f(p_2) = C_F \int_k \gamma_\mu S_f(k_2) \gamma_\nu D^{\mu\nu}_{ff'}(k)\,. \tag{3.7}$$

We note that, in contradistinction to $\Sigma_f(p_1)$ and $\Sigma_f(p_2)$, the $\widetilde{\Sigma}_f(p_1)$ and $\widetilde{\Sigma}_f(p_2)$ in (3.7) contain a non-diagonal $D^{\mu\nu}_{ff'}(k)$, which thwarts the interpretation of these quantities as genuine self-energies. Evidently, this mismatch is the manifestation of the WTI violation associated with the use of the kernel $I_{ff'}(q^2)$ when $f \neq f'$.

A way to quantify this violation is to study the quantitative difference between the components of the $S_f(p)$ computed using $\Sigma_f(p)$, and the same $S_f(p)$ computed using $\widetilde{\Sigma}_f(p)$ for all possible $I_{ff'}(q^2)$. In particular, if we fix $f = u$, we may first compute $\Sigma_u(p)$ using the correct kernel I_{uu}; we will denote the resulting quark propagator by $\Sigma_{uu}(p)$, where the additional subscript "u" indicates precisely that I_{uu} was used in the computation. Then, we compute $\Sigma_u(p)$ using instead $\widetilde{\Sigma}_u(p)$, which, depending on the value of f', may contain I_{us}, I_{uc}, or I_{ub}; this gives rise to three versions of $\Sigma_u(p)$, which we denote by $\Sigma_{us}(p)$, $\Sigma_{uc}(p)$, and $\Sigma_{ub}(p)$, respectively. Employing the standard decomposition given in (2.9), we will denote the corresponding Dirac components of the above quark propagators by $A_{uu}(p^2)$, $A_{uf'}(p^2)$, and $B_{uu}(p^2)$, $B_{uf'}(p^2)$, and the resulting versions of the u quark mass by $\mathcal{M}_{uu}(p^2)$ and $\mathcal{M}_{uf'}(p^2)$, with $f' = s, c, b$.

With the above ingredients in hand, we next introduce the point-wise percentage errors $(\delta A)_{uf'}(p^2)$ and $(\delta\mathcal{M})_{uf'}(p^2)$, defined as

$$(\delta A)_{uf'}(p^2) = \frac{2\,|A_{uu}(p^2) - A_{uf'}(p^2)|}{A_{uu}(p^2) + A_{uf'}(p^2)} \times 100\%\,,$$
$$(\delta\mathcal{M})_{uf'}(p^2) = \frac{2\,|\mathcal{M}_{uu}(p^2) - \mathcal{M}_{uf'}(p^2)|}{\mathcal{M}_{uu}(p^2) + \mathcal{M}_{uf'}(p^2)} \times 100\%\,, \tag{3.8}$$

for $f' = s, c, b$. The curves for $(\delta A)_{uf'}(p^2)$ and $(\delta\mathcal{M})_{uf'}(p^2)$, obtained from the appropriate treatment of the gap equation, are shown in Fig. 5. We see that in the worst case, involving the quarks with the largest mass disparity, $f = u$ and $f' = b$, the maximum error in the computation of the quark wave-function is slightly over 3% (left panel). The maximum discrepancy in the computation of the constituent quark masses occurs again for the case $f = u$ and $f' = b$, and is about 9% (right panel).

As an illustration, we computed the mass of the heavy light meson D using propagators for both the u and c quarks constructed with $\Sigma_{uc}(p)$, i.e., both dressed using the off-diagonal kernel I_{uc}. This yields a mass of 1.99 GeV, compared to the 1.93 GeV obtained in our previous study using diagonal kernels for the propagators [32], i.e., an error of about 3%.

4 Quark-photon vertex

The quark-photon vertex is a crucial ingredient in the study of the electromagnetic interaction of hadrons [10,19,22,23], and has been studied in isolation in a series of works [7,57–60].

Just as the electron-photon vertex known from QED, the quark-photon vertex $\Gamma^f_\mu(p_1, p_2)$ satisfies the fundamental WTI

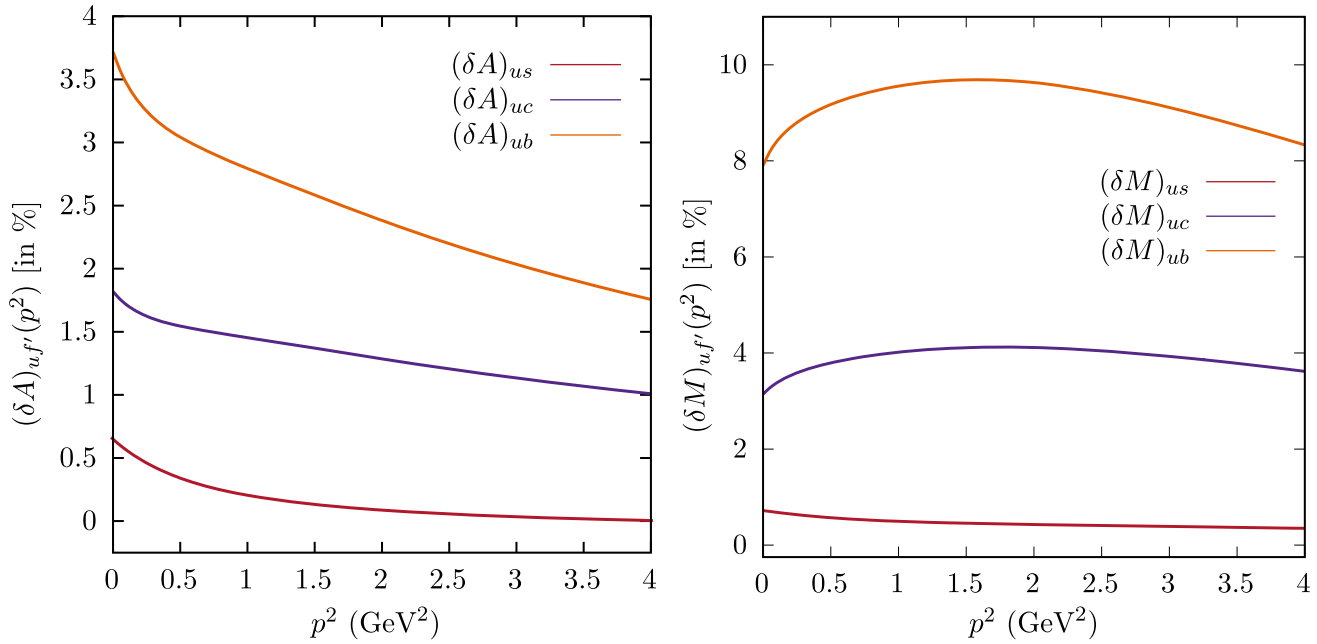

Fig. 5 he relative point-wise percentage errors defined in (3.8), computed for the quark dressing functions $A(p^2)$ (left panel), and the quark masses $M(p^2)$ (right panel)

$$q^\mu \Gamma^f_\mu(p_1, p_2) = i S_f^{-1}(p_2) - i S_f^{-1}(p_1)\,. \tag{4.1}$$

It is now straightforward to establish the compatibility of the kernel $I_{ff}(q^2)$ with the local $U(1)$ symmetry, encoded in the WTI of (4.1). At the level of the bare vertex SDE ($Z_2 = 1$), one contracts by q^μ both sides of (2.13), and uses the r.h.s. of (4.1) under the integral sign of (2.13), namely

$$\begin{aligned} q^\mu \Gamma^f_\mu(p_1, p_2) &= \not{p}_1 - \not{p}_2 - i C_F \int_k \gamma_\alpha S_f(k_1)[S_f^{-1}(k_2) \\ &\quad - S_f^{-1}(k_1)] S_f(k_2)\, \gamma_\beta D^{\alpha\beta}_{ff}(k) \\ &= i\left[i\not{p}_2 + m_f + C_F \int_k \gamma_\alpha S_f(k_2) \gamma_\beta D^{\alpha\beta}_{ff}(k)\right] \\ &\quad i\left[i\not{p}_1 + m_f + C_F \int_k \gamma_\alpha S_f(k_1) \gamma_\beta D^{\alpha\beta}_{ff}(k)\right], \end{aligned} \tag{4.2}$$

which, by virtue of (2.10), is precisely the WTI of (4.1). The preservation of the $U(1)$ gauge symmetry ensures charge conservation, which is crucial for the veracious calculation of hadronic form factors. Note, in addition, that the requirement that the WTI of (4.1) be valid *after* renormalization imposes the well-known relation $Z_1 = Z_2$, where Z_1 denotes the renormalization constant of the quark-photon vertex; this equality has already been enforced at the level of the vertex SDE in (2.13), where Z_1 has been replaced by Z_2.

The vertex $\Gamma_\mu(p_1, p_2)$ may be naturally decomposed into two parts,

$$\Gamma^\mu(p_1, p_2) = \Gamma^\mu_{\rm BC}(p_1, p_2) + \Gamma^\mu_{\rm T}(p_1, p_2)\,, \tag{4.3}$$

where the so-called "Ball-Chiu" part, $\Gamma^\mu_{\rm BC}(p_1, p_2)$, saturates the WTI of (4.1), while the transverse part, $\Gamma^\mu_{\rm T}(p_1, p_2)$, satisfies $q_\mu \Gamma^\mu_{\rm T}(p_1, p_2) = 0$. According to the construction of [61], the form factors comprising $\Gamma^\mu_{\rm BC}(p_1, p_2)$ are expressed entirely in terms of the quark functions $A(p^2)$ and $B(p^2)$ appearing in (2.9). In particular, introducing for convenience the kinematic variables $u = (p_1 + p_2)/2$ and $q = p_1 - p_2$, we have

$$\Gamma^\mu_{\rm BC}(q, u) = \lambda_1 \gamma^\mu + 2\lambda_2\, u^\mu \not{u} + 2i\lambda_3\, u^\mu + i\lambda_4 [\gamma^\mu, \not{q}]\,, \tag{4.4}$$

with the form factors given by

$$\begin{aligned} \lambda_1 &= \frac{A(p_1^2) + A(p_2^2)}{2}\,, \quad \lambda_2 = \frac{A(p_1^2) - A(p_2^2)}{p_1^2 - p_2^2}\,, \\ \lambda_3 &= \frac{B(p_1^2) - B(p_2^2)}{p_1^2 - p_2^2}\,, \quad \lambda_4 = 0\,. \end{aligned} \tag{4.5}$$

The transverse component $\Gamma^\mu_{\rm T}(p_1, p_2)$ may be expanded as

$$\Gamma^\mu_{\rm T}(q, u) = \sum_{i=1}^{8} h_i(q, u)\, \tau_i^\mu, \tag{4.6}$$

where the τ_i^μ are the elements of an eight-dimensional basis, and the $h_i(q,u)$ denote the associated form factors. Specifically, we employ the basis of [62], whose elements are given by

$$\begin{aligned}
\tau_1^\mu &= t_{qq}^{\mu\nu}\gamma_\nu, & \tau_2^\mu &= t_{qq}^{\mu\nu}\,(u\cdot q)\,\frac{i}{2}[\gamma_\nu, \not{u}],\\
\tau_3^\mu &= \frac{i}{2}[\gamma^\mu, \not{q}], & \tau_4^\mu &= \frac{1}{6}[\gamma^\mu, \not{u}, \not{q}],\\
\tau_5^\mu &= i t_{qq}^{\mu\nu} u_\nu, & \tau_6^\mu &= t_{qq}^{\mu\nu} u_\nu \not{u},\\
\tau_7^\mu &= t_{qu}^{\mu\nu}\,(u\cdot q)\,\gamma_\nu, & \tau_8^\mu &= t_{qu}^{\mu\nu}\frac{i}{2}\left[\gamma_\nu, \not{u}\right],
\end{aligned} \tag{4.7}$$

where we used the projector $t_{ab}^{\mu\nu} = (a\cdot b)\,\delta^{\mu\nu} - b^\mu a^\nu$, and the triple commutator is defined as $[A,B,C] = [A,B]C + [B,C]A + [C,A]B$, with $[A,B,A] = 0$. It is understood that all form factors introduced above carry a flavour index "f", which has been suppressed for simplicity.

Note that a key advantage of the decomposition in (4.3) is that it enables a separation of the transverse components with respect to the total momentum q. This is especially relevant for a time-like photon, where the quark-photon vertex develops vector meson bound-state poles (e.g., at $q^2 = -M_\rho^2$). These poles reside exclusively in the transverse components, while the time-like domain may also feature non-resonant singularities originating from the analytic structure of the quark propagator [58,63].

5 Results and discussion

In this section we present the numerical results for the BS amplitude and quark-photon vertex. Once these elements have been obtained, the current J_μ can be calculated from (2.2), and the EFF of pseudoscalar particles may be subsequently extracted.

5.1 Numerical inputs

The current quark masses have been fixed to the following values:

$$\begin{aligned}
&m_{u/d} = 0.005\,\text{GeV}, \quad m_s = 0.094\,\text{GeV}, \quad m_c = 1.1\,\text{GeV},\\
&m_b = 3.5\,\text{GeV},
\end{aligned} \tag{5.1}$$

at the renormalization point $\mu = 4.3$ GeV. Furthermore, the parameter η that controls the routing of the total momentum p_{av} in (2.4) has been fixed to the following values, which depend on the quark content of the meson:

$$\begin{aligned}
&\eta_{us} = 0.47, \quad \eta_{cb} = 0.41, \quad \eta_{sc} = 0.38, \quad \eta_{sb} = 0.25,\\
&\eta_{cd} = 0.24, \quad \eta_{ub} = 0.16.
\end{aligned} \tag{5.2}$$

These values have been fixed to avoid singularities in the quark propagator and to facilitate the numerical calculations; for a further discussion, see Sect. 5.3. The resulting quark dressing functions $A(p)$ and $M(p)$ are the same as those computed in Fig. (5) of Ref. [32]. Here, it is important to remark that when employing these fixed values for $\eta_{ff'}$ the light mesons, together with the heavy light D and D_s, can be computed numerically onshell. On the other hand, for the B, B_s and B_c we employed a parametrization of the quark propagator in terms of complex conjugate poles, as described in [32].

5.2 Results and comparison with the literature

(i) **BS amplitudes.** To compute the BS amplitude from (2.11), we employ standard methods where the integral equation is reformulated as an eigenvalue problem. The physical solutions correspond to mass-shell points given by $P^2 = -M^2$. In our numerical implementation, the BS amplitude is expanded using a basis of 8 Chebyshev polynomials. Figure 6 displays the resulting subamplitudes $\chi_i^{ff'}$ for the pion and the D_s meson, projected onto the leading Chebyshev moment.

(ii) **Form factors for the quark-photon vertex.** For the calculation of spacelike hadron form factors, the quark-photon vertex is required in the region $q^2 > 0$. The solution of (2.13), unlike the homogeneous case, does not correspond to an eigenvalue problem. Instead, the equation is a linear integral equation driven by the bare vertex, which after discretization reduces to a system of linear equations where the interaction kernel defines the matrix structure. Such systems can be solved using "LU decomposition", factorizing the kernel matrix into lower and upper triangular parts for efficient inversion [64]. In Figs. 7 and 8 we present the full structure of the vertex for u and s quarks. As a consistency check, we have verified that our numerical results from the WTI solution from (4.5) are identical to those obtained from the vertex SDE. On the other hand, the transverse components are consistent with previous studies [58,65].

(iii) **Electromagnetic form factors.** Moving to the EFFs in Figs. 9 and 10, we note that our results are correctly normalized, satisfying $F(0) = 1$ for electrically charged particles, and $F(0) = 0$ for neutral mesons, as required by the vector WTI.

The left panel of Fig. 9 shows that our result for the pion electromagnetic form factor is in excellent agreement with experimental measurements. Similarly, the right panel of Fig. 9 shows that our computation for the kaon electromagnetic form factor is consistent with the available experimental data. Furthermore, our results for the D and D_s mesons exhibit a similar qualitative behavior to that observed between the pion and kaon, see Fig. 10, where the inclusion of a strange

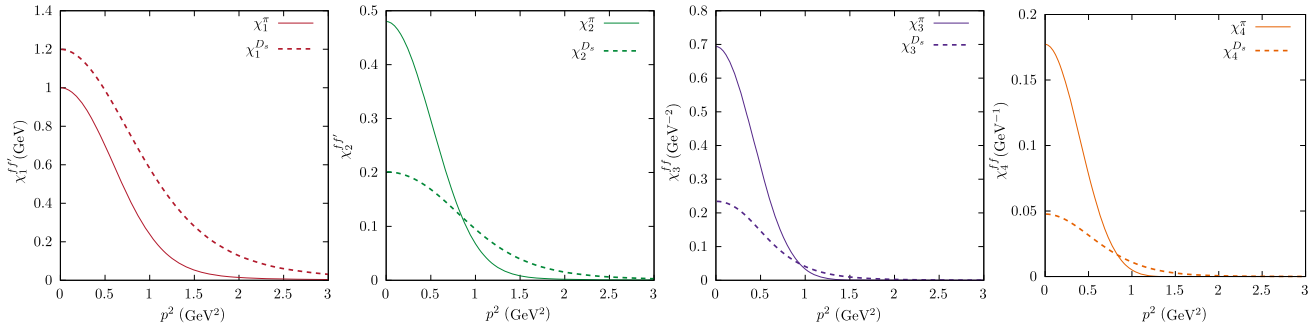

Fig. 6 The BS amplitude for the pion (solid lines) and for the D_s (dashed lines). We have set $\chi_i^{\pi} := \chi_i^{u\bar{d}}$ and $\chi_i^{D_s} := \chi_i^{c\bar{s}}$, where the general amplitude $\chi_i^{ff'}$, indicating the specific quark content, has been introduced in (2.12). For easier comparison, all BS amplitudes are rescaled such that $\chi_1^{\pi}(0) = 1$

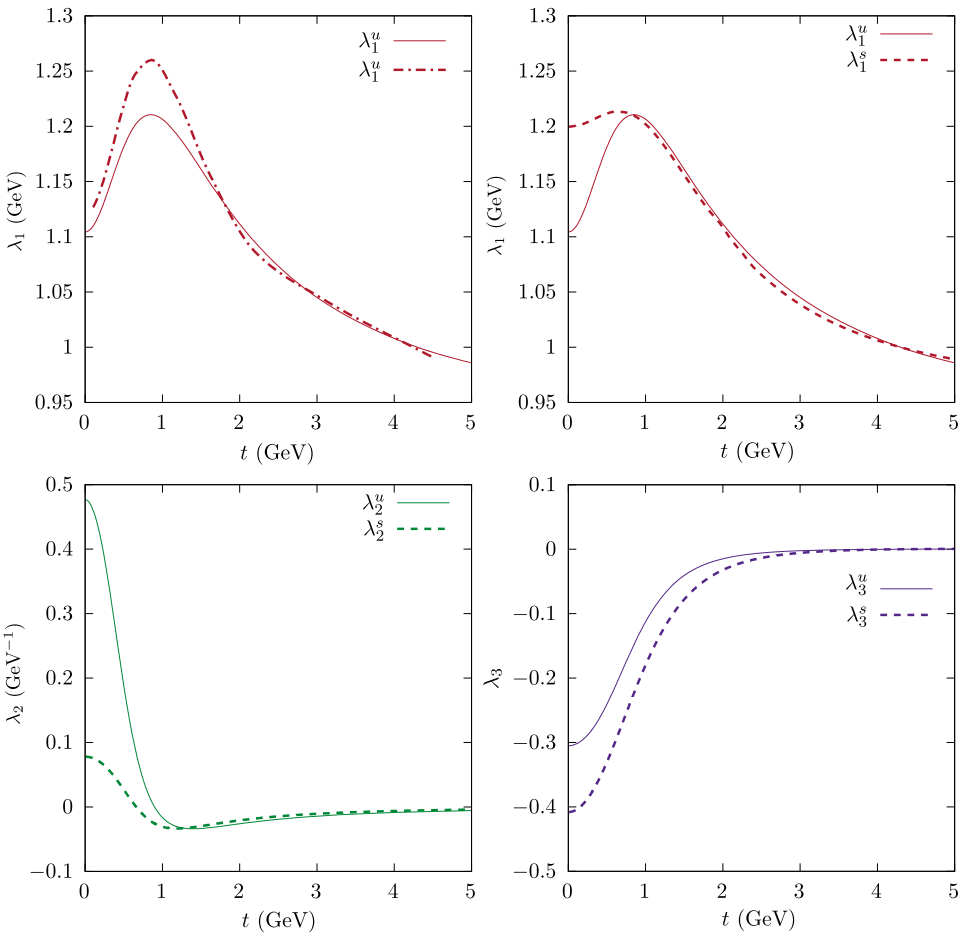

Fig. 7 Longitudinal form factors of the quark-photon vertex. Upper-left: the up-quark form factors obtained using the interaction of (2.6) (solid line) compared to the RL result of [58] (dash-dotted lines). Upper right: up-quark (solid line) and strange quark (dashed line) form factor λ_1. Bottom panel: up-quark (solid line) and strange quark (dashed line) form factor λ_2. and λ_3

quark in the meson's quark content leads to a slight difference between the form factor of $D(c\bar{d})$ and $D_s(c\bar{s})$, reflecting the influence of the quark mass. A similar trend is evident in the comparison between the $B(u\bar{b})$ and $B_c(c\bar{b})$ form factors, where the presence of a lighter quark enhances the mass asymmetry, resulting in a more pronounced variation in the behavior of the form factor.

In the case of the η_c and η_b mesons, when both quark and antiquark contributions are included, the total electromagnetic form factor vanishes identically due to charge conjugation. Nevertheless, structural information can still be extracted by computing the form factor associated with a single quark contribution from (2.5). Our results indicate that the electromagnetic form factor for the η_b exhibits a noticeably slower decrease with increasing momentum transfer compared to the η_c. We emphasize that the single-quark contributions shown for η_c and η_c are *not* physical observables; they are included as useful theoretical reference quantities that can

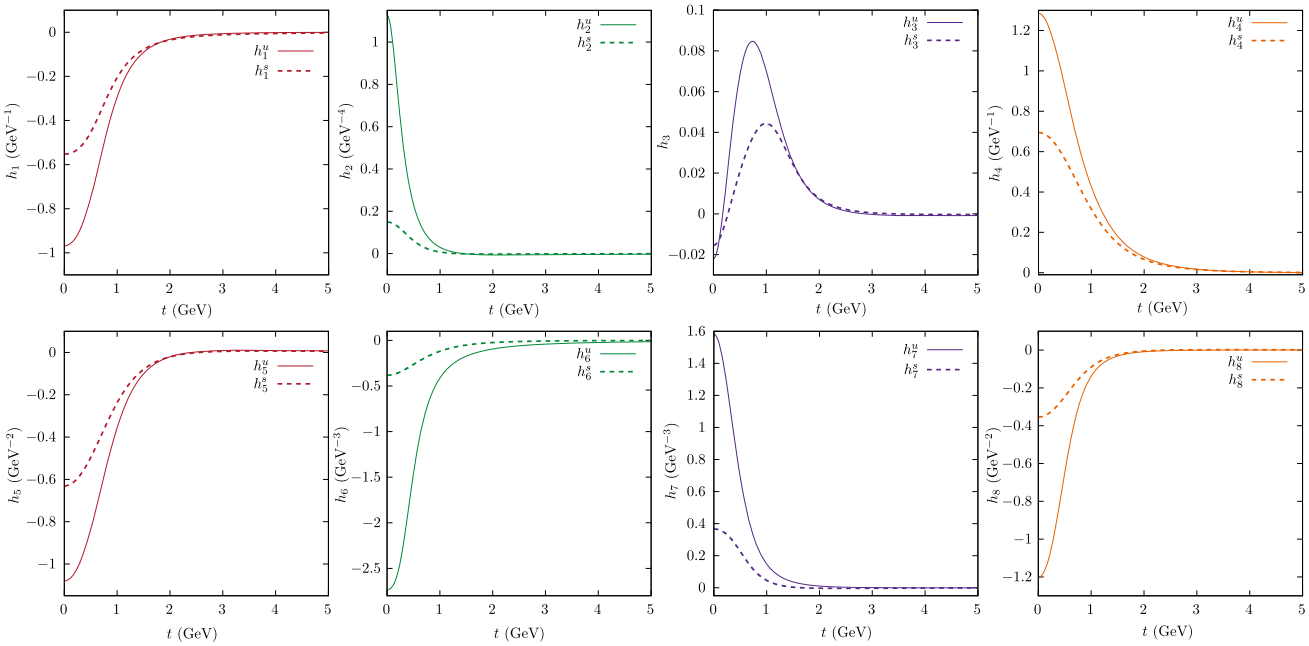

Fig. 8 Transverse form factors of the quark-photon vertex using the interaction from (2.6) for up quark (solid lines) and strange quark (dashed lines)

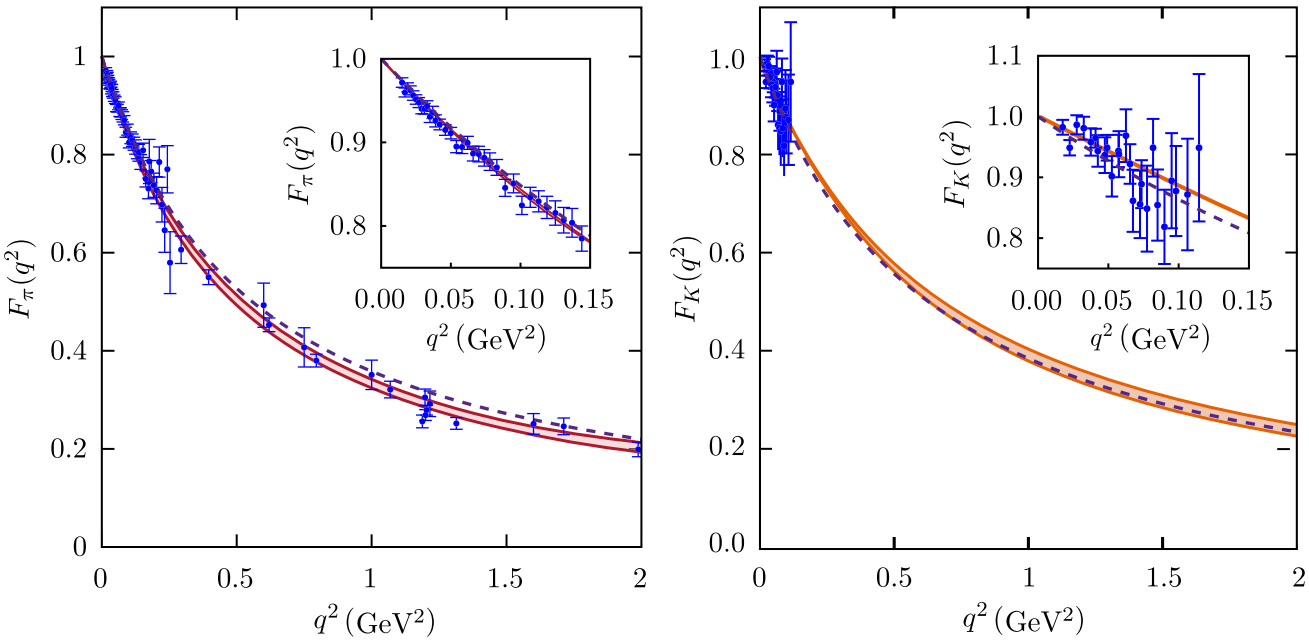

Fig. 9 Computed pion (left) and kaon (right) electromagnetic form factor for a space-like photon (solid lines), compared with the available experimental data [66–71] and with the results from the weighted-RL [19] (dashed-line). The insets offer a closer look at the infrared region of momenta, where most of the experimental points are accumulated. The band on our calculations originates from the variation of the modified Taylor coupling $\tilde{\alpha}_T(q^2)$, shown in Fig. 3

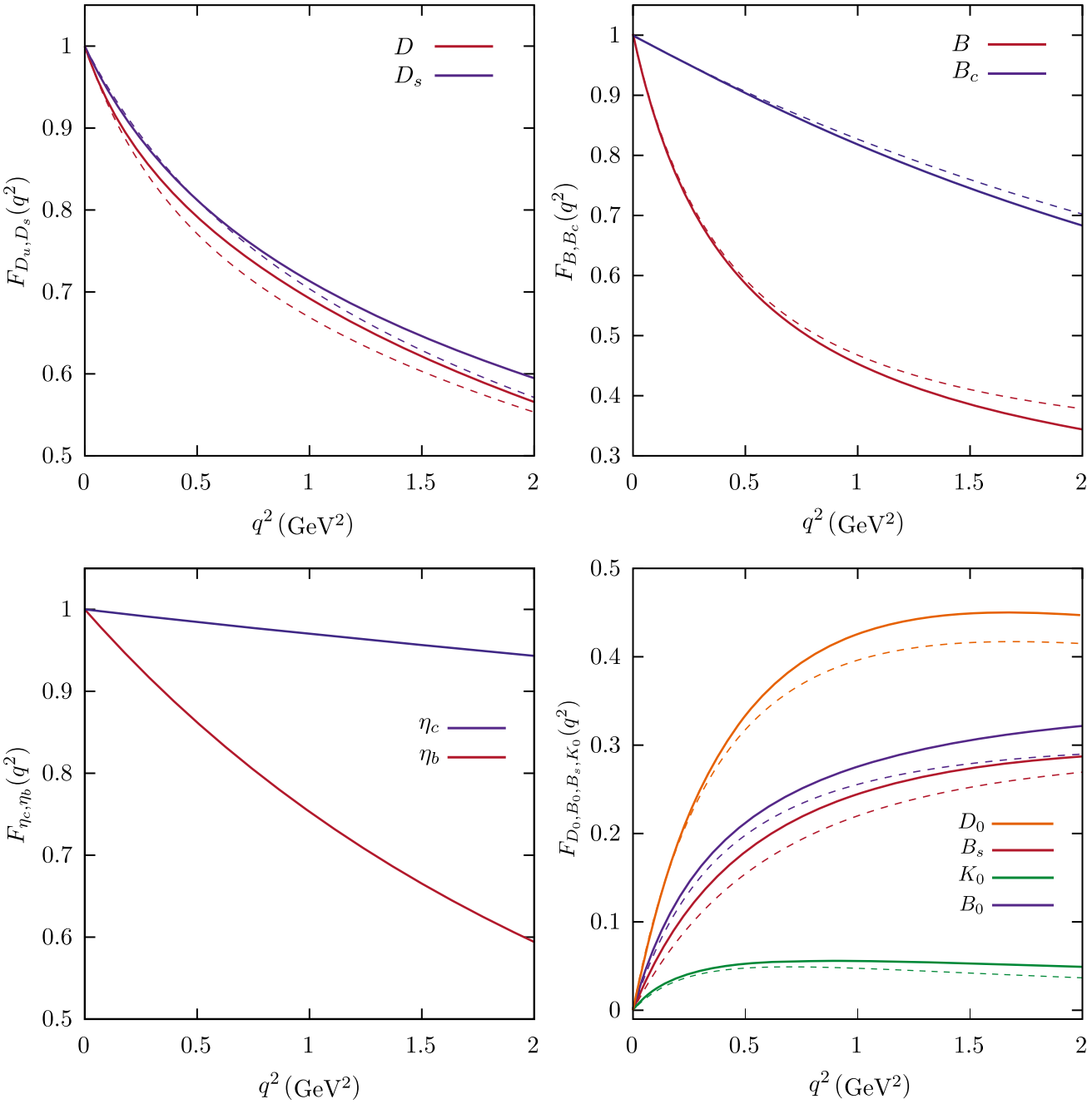

Fig. 10 Computed electromagnetic form factors (solid lines) for mesons interacting with a space-like photon compared with the results from [19] (dashed-line). Results are shown for: D and D_s (upper left), B and B_c (upper-right), η_c and η_b (bottom-left), and for K_0, D_0, B_0 and B_s (bottom-right). Note that the curves for the η_c and η_b mesons correspond to the single–quark contributions; as explained in the text, these contributions are *not* physical observables, but could serve as theoretical benchmarks for heavy–heavy systems

serve as benchmarks across different theoretical approaches (e.g. lattice QCD, functional methods, quark models, etc.) when analyzing heavy–heavy pseudoscalars.

(iv) **Charge radii.** The charge radius can be determined from the derivative of the electromagnetic form factor evaluated at $q^2 = 0$:

$$\langle r^2\rangle = -6\frac{dF(q^2)}{dq^2}\Big|_{q^2=0}. \tag{5.3}$$

The computed charge radii for different pseudoscalar mesons are presented in Tables 1 and 2, where they are compared with experimental measurements, as well as predictions from the Contact Interaction (CI) model [72], the Algebraic model

Table 1 Charge radius results for light and charm pseudoscalar mesons. All results are given in fm. Note that the imaginary factor "i" has been used when the squares of the reported radii are negative. Uncertainties for the radii of the π and K mesons are shown, obtained from a $\pm\sigma$ variation of the parameters in the modified Taylor coupling, see Sect. 5.3. The values taken from the literature are supplied with uncertainties only when explicitly reported in the original references

Radius (fm)	π	K	K^0	D	D_0	D_s
This work	0.656(5)	0.568(4)	0.270i	0.428	0.542i	0.368
Experiment [78]	0.659(4)	0.560(30)	0.277(18)i	–	–	–
LQCD [74,75]	0.656(11)	–	–	0.450(24)	–	0.465(57)
Data driven [76,77]	0.655(18)	0.599(4)	0.245(8)i	–	–	–
Weighted-RL [19]	0.646	0.608	0.253i	0.435	0.556i	0.352
Light front [45]	0.668(35)	0.610(20)	0.302(22)i	0.411(15)	0.534(26)i	0.301(11)
AM [73]	–	–	–	0.680		0.372
CI [72]	0.45	0.42	–	–	–	0.26

Table 2 Charge radius predictions for bottom and heavy pseudoscalar mesons. All results are given in fm. Note that the imaginary factor "i" has been used when the squares of the reported radii are negative. We remind the reader that the η_c and η_b results correspond to single–quark contributions, which are not physical observables but serve as theoretical benchmarks for heavy–heavy systems

Radius (fm)	B	B_0	B_s	B_c	η_c	η_b
This work	0.631	0.442i	0.330i	0.213	0.267	0.082
Weighted-RL [19]	0.619	0.435i	0.337i	0.219	–	–
Light front [45]	0.564(22)	0.396(16)i	0.281(13)i	0.189(10)	–	–
AM [73]	0.926	–	0.345i	0.217	–	–
CI [72]	0.34	0.36i	0.24i	0.17	0.20	0.07

(AM) [73], Lattice QCD (LQCD) [74,75], Data driven [76,77], Light front [45], and the weighted-RL approach of [19].

Our results for the π^+, K^+, and K^0 mesons are in very good agreement with experimental values, showing small deviations of 0.45, 1.42, and 2.5%, respectively.

Comparing our results with those from other approaches, we observe some differences. The CI model underestimates the charge radii of the pion and kaon, predicting values of 0.450 fm and 0.420 fm, respectively, which are significantly smaller than both experimental measurements and our own results. This underestimation is also evident in the predictions for heavy-light mesons, where, for instance, the D_s meson radius is given as 0.260 fm, notably lower than our 0.368 fm. Nevertheless, the overall qualitative behavior is consistent with our findings.

The Algebraic model yields a charge radius of 0.680 fm for the D meson, which is substantially larger than both our prediction (0.428 fm) and lattice QCD results (0.450 fm). Additionally, this model exhibits a significant difference between the D and D_s mesons, with a predicted charge radius of 0.372 fm for the latter, whereas our results suggest that these two mesons should have comparable charge radii.

For heavy-light mesons, our results exhibit a similar overall behavior compared to the weighted-RL investigated in [19]. In particular, our predictions for the B and B_s mesons, 0.631 fm and 0.330i fm, respectively, are in close agreement with the corresponding weighted-RL values of 0.619 fm and 0.337i fm. The most noticeable discrepancies arise in the light meson sector, where some variations in the charge radii are observed.

Finally, it is interesting to note that lattice QCD is the only approach that obtains a larger central value for the charge radius of the D_s meson than for the D meson. Nevertheless, the error for both particles is rather considerable.

5.3 Error analysis

In order to ascertain the robustness of our key results, in this subsection we study their stability under variations of the inputs, as well as of the parameters entering in the calculations.

5.3.1 Varying the interaction strength

The central quantity in this entire approach is the interaction strength $\mathcal{I}_{ff'}(q^2)$, defined in (2.6), which, as explained in detail in Sect. 2.2, enters in all dynamical equations. The most prominent ingredient of $\mathcal{I}_{ff'}(q^2)$ is the modified Taylor coupling, $\tilde{\alpha}_T(q^2)$, which is constructed using the standard Taylor coupling, $\alpha_T(q^2)$, as the basic quantity of reference. In particular, $\alpha_T(q^2)$ is taken from the $N = 2+1+1$ lattice analysis of [50], and has distinct error bars associated with

Table 3 Values of the parameters defining the modified Taylor coupling $\tilde{\alpha}_T(q^2)$ from (5.4). The central set corresponds to the best fit to the lattice-QCD data from [32], while the "Top" and "Bottom" sets represent variations of $+\sigma$ and $-\sigma$, respectively. Additionally, we employed $a_3 = 10.72\ \text{GeV}^{-2}$, $a_4 = -2.5\ \text{GeV}^{-4}$ and $a_5 = 29.02\ \text{GeV}^{-6}$, Λ_T=0.5 GeV, $\Lambda_0 = 1$ GeV and $\beta_0 = 11 - 2n_f/3$ ($n_f = 4$)

	a_0 (GeV^{-2})	a_1 (GeV^{-4})	a_2 (GeV^{-4})
Top	10.85	24.19	28.44
Central	10.35	23.69	27.94
Bottom	9.85	23.19	27.44

all available points; as may be seen in the plot of Fig. 3, these errors propagate finally into $\tilde{\alpha}_T(q^2)$. We emphasize once more that the determination of $\tilde{\alpha}_T(q^2)$ does not involve any adjustable parameters. For the purposes of our analysis, we employ the following fitting function for $\tilde{\alpha}_T(q^2)$,

$$\tilde{\alpha}_T(q^2) = \frac{a_0 q^2 + a_1 q^4 \ln\left(1 + \frac{\Lambda_0^2}{q^2}\right) + a_2 q^4}{1 + a_3 q^2 + a_4 q^4 + a_5 q^6} + \frac{4\pi q^6}{\beta_0 \left(\Lambda_0^6 + q^6 \ln \frac{q^2}{\Lambda_T^2}\right)}, \tag{5.4}$$

which describes very accurately the lattice data of Fig. 3 [32].

To provide an estimate of the numerical uncertainty associated with our results for the pion and kaon electromagnetic form factors, we varied the parameters entering in the $\tilde{\alpha}_T(q^2)$ of (5.4) by one standard deviation ($\pm\sigma$) around their central values. The corresponding values of the parameters are displayed in Table 3. The resulting variation is illustrated in Fig. 3, where the dashed curve corresponds to the central parametrization of $\tilde{\alpha}_T(q^2)$ employed in [32], and the shaded band indicates the effect of this variation.

The propagated uncertainty affects the bound-state masses, the BS amplitudes, the quark–photon vertex, and, consequently, the electromagnetic form factors. The resulting masses for the pion and kaon are $m_\pi = 0.139(2)$ GeV and $m_K = 0.495(2)$ GeV. For the BS amplitudes shown in Fig. 6, the variation induced by the coupling uncertainty is at the level of approximately 2%, while the quark–photon vertex varies by about 1%.

The final propagation of all these errors at the level of the EFF for the pion and kaon is shown in the bands of Fig. 9. The extracted charge radii, $r_\pi = 0.656(5)$ fm and $r_K = 0.568(4)$ fm, remain in excellent agreement with experimental measurements.

5.3.2 *Varying the renormalization scale μ*

On general grounds, current matrix elements, such as the $J^\mu(p_{\text{av}}, q)$ considered here, do not depend on the renormalization scale μ employed in intermediate calculations [23]. Of course, given that our framework contains truncations and approximations, it is essential to test explicitly the response of the obtained results under variations of the scale μ.

The natural point of departure for such a study is the quark gap equation of (2.10), in conjunction with the BSE in (2.11). Let us focus on the set of current quark masses given in (5.1), which have been determined at the renormalization point $\mu = 4.3$ GeV. In particular, for the case of m_u, the determination proceeds as follows [32,79]. The gap equation of (2.10) is renormalized at $\mu = 4.3$ GeV, by imposing the MOM condition $A_u(\mu = 4.3\,\text{GeV}) = 1$, which fixes the value of the renormalization constant Z_2. Then, the gap equation is solved for a variety of values for m_u, yielding a sequence of solutions for $A_u(p)$, $B_u(p)$, and $\mathcal{M}_u(p)$. In continuation, these solutions are fed into the BSE of (2.11), which yields a sequence of values for the pion mass. At this point, we single out the value of m_u for which the pion mass assumes its observed value, $m_\pi = 139$ MeV. An identical procedure is employed for determining m_s, m_c, and m_b, using as benchmarks the masses of the kaon, η_c, and η_b.

The procedure described above may be repeated for different values of μ; in particular, we have used the following values, $\mu \in \{4.3, 3.0, 2.5, 2.0\}$ GeV.

Upon completion of these variations, the following observations are in order:

(*i*) The constituent masses of the quarks, $\mathcal{M}(p)$, are completely μ-independent, as expected. The case of $\mathcal{M}_u(p)$ is shown in the left panel of Fig. 11.

(*ii*) The values of the current masses of the up, m_u, are shown in Table 4. Note that, in general, the current masses satisfy the relation $\mathcal{M}(\mu) = m$, imposed by the renormalization condition $m_R = Z_m m_0$, as may be seen in the inset of the left panel of Fig. 11.

(*iii*) The variation of the renormalization constant Z_2 for different values of μ is shown in Table 4, while the family of up quark wave functions, $A_u(p)$, is shown in the right panel of Fig. 11. As a self-consistency check, we note that the bare $A_0(p)$ and the renormalized $A_R(p, \mu)$ are related by $A_0(p) = Z_2^{-1}(\mu) A_R(p, \mu)$. Since $A_0(p)$, being a bare quantity, does not dependent on μ, when each solution $A_R(p, \mu)$ is divided by its corresponding $Z_2(\mu)$, they should all collapse to a single curve. As may be verified from the inset in the right panel of Fig. 11, this is indeed what happens, at a high level of accuracy. This serves as a useful self-consistency check, indicating that the solutions of the gap equation respond under variations of the renormalization scale exactly as expected on theoretical grounds.

(*iv*) The ingredients obtained from the gap equation, for different values of μ, are subsequently substituted into the BSE of (2.11), in order to obtain the bound-state masses and amplitudes. It turns out that the results are completely stable, both at the level of the BS amplitudes as well as the

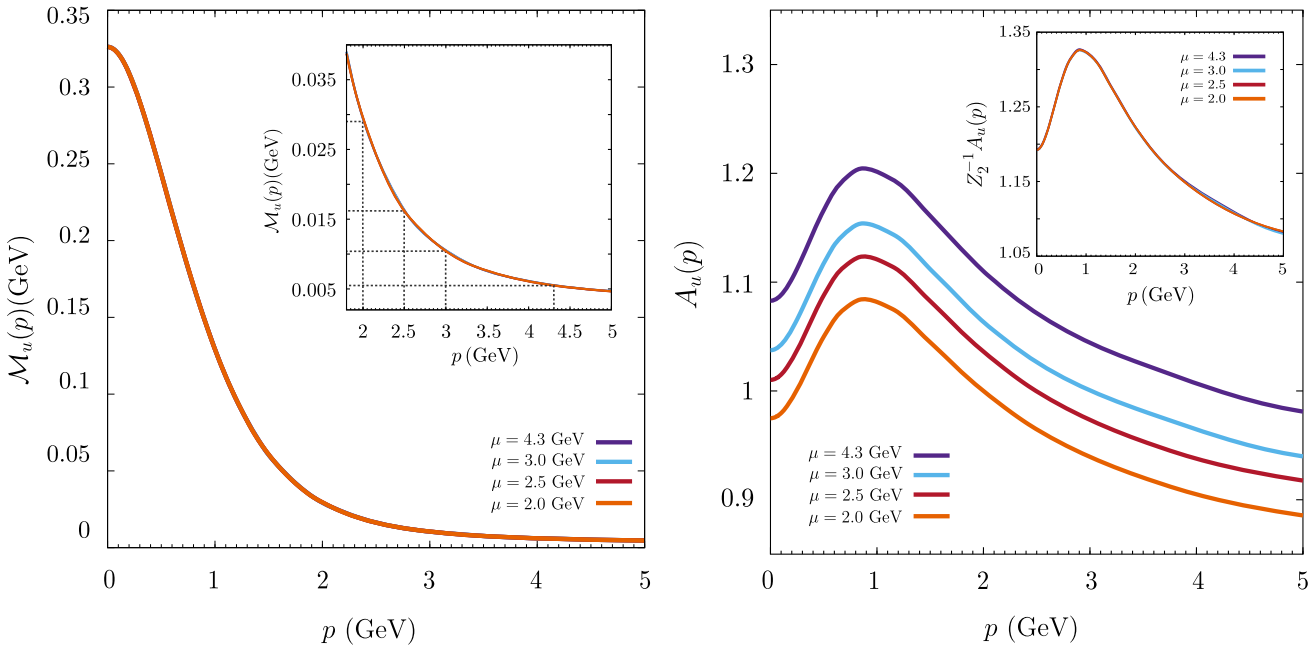

Fig. 11 Left: The mass $\mathcal{M}_u(p)$ computed for the four values of μ indicated; the μ-independence of $\mathcal{M}_u(p)$ is evident. In the inset we display the values of the current quark masses, using the property $\mathcal{M}_u(\mu) = m_u$. Right: The quark wave function $A_u(p)$ obtained for various values of μ. As expected on formal grounds [see point (*iii*)], when divided by the corresponding $Z_2(\mu)$, all curves collapse essentially to one (inset)

Table 4 Computed values for the renormalized constant Z_2 for different values of μ with the respective up quark mass

μ (GeV)	4.3	3.0	2.5	2.0
Z_2	0.90	0.88	0.86	0.83
m_u (GeV)	0.0052	0.010	0.016	0.029

masses. For instance, in the case of the pion mass, one finds a variation of less than one per mil, with comparable numbers for the other mesons. This stability may be ultimately traced back to the RGI nature of the BSE kernel [32]; specifically, the BSE kernel maintains its form invariant before and after renormalization, namely $S_0 S_0 D_0 = S_R S_R D_R$, a property that is tantamount to complete μ-independence.

The final step is to confirm numerically that the μ-dependences carried by the $A(p)$ cancel when they are inserted in the formulas that furnish the EFFs, such as (2.2). These cancellations are driven by the fundamental WTI in (4.1), connecting the inverse quark propagator with the quark-photon vertex. The numerical analysis reveals that, indeed, the μ-dependences from the $A(p)$ are nearly perfectly compensated by those contained in the vertex form factors.

The final upshot of these considerations is that the observables computed change by less than one per mil under the considered variations of the renormalization scale.

5.3.3 *Varying the momentum routing of the BSE*

The parameter η, introduced in (2.4), determines the distribution of the total momentum among the quark and antiquark in the BSE. As a general practice, the values of the η are chosen in such a way as to avoid kinematic singularities in the quark propagators, especially in systems displaying large quark mass disparities. As discussed in [19,65,80,81], the precise choices used for the routing parameter η have no impact on physical observables. In practice, varying η from its "optimal" value simply means that a finer integration grid is required for reaching a given level of precision, thus increasing the computational cost. This logistical complication aside, all calculated observables remain unchanged.

The values for the parameters η quoted in (5.2) minimize the computational cost, requiring the least number of Chebyshev polynomials (8) for the treatment of the corresponding BSEs. Deviations from these selected values forces the use of a larger number of such polynomials, in order to maintain the desired numerical accuracy. Our variations show that, depending on the computational details, the number of required polynomials varies between 10 to 12, leading to a 50% increase in the computational time.

6 Conclusions

In this work, we have applied the Bethe–Salpeter framework to the computation of EFFs of heavy–light pseudoscalar mesons by implementing a flavour–dependent interaction kernel. The computed EFFs for light mesons (π and K) show excellent agreement with experimental data, thereby validating the consistency of the approach. In the heavy–light sector, where experimental and lattice QCD results for form factors are not yet available, we provide predictions. In particular, our estimates of the charge radii are in good agreement with existing theoretical studies, offering valuable benchmarks for forthcoming lattice and experimental efforts.

Furthermore, the present framework can be naturally extended to the study of vector mesons, such as the ρ and K^*, for which EFFs provide complementary insight into internal meson structure beyond spin-zero systems. Beyond mesons, the formalism can also be applied to baryons, which will be investigated in the future.

Acknowledgements The authors thank Yin-Zhen Xu for useful communications. The work of A.S.M. and J.P. is funded by the Spanish MICINN grants PID2020-113334GB-I00 and PID2023-151418NB-I00, the Generalitat Valenciana grant CIPROM/2022/66, and CEX2023-001292-S by MCIU/AEI. J.P. is supported in part by the EMMI visiting grant of the ExtreMe Matter Institute EMMI at the GSI, Darmstadt, Germany. J.M.P. is funded by the Deutsche Forschungsgemeinschaft (DFG, German Research Foundation) under Germany's Excellence Strategy EXC 2181/1 - 390900948 (the Heidelberg STRUCTURES Excellence Cluster) and the Collaborative Research Centre SFB 1225 - 273811115 (ISOQUANT).

Data Availability Statement Data will be made available on reasonable request. [Authors' comment: The datasets generated during and/or analysed during the current study are available from the corresponding author on reasonable request.].

Code Availability Statement Code/software will be made available on reasonable request. [Authors' comment: The code/software generated during and/or analysed during the current study is available from the corresponding author on reasonable request.].

Funded by SCOAP[3].

References

1. E.E. Salpeter, H.A. Bethe, Phys. Rev. **84**, 1232 (1951). https://doi.org/10.1103/PhysRev.84.1232
2. M. Gell-Mann, F. Low, Phys. Rev. **84**, 350 (1951). https://doi.org/10.1103/PhysRev.84.350
3. H.A. Bethe, E.E. Salpeter, Quantum mechanics of one- and two-electron systems. in *Atoms I/Atome I* (Springer Berlin Heidelberg, Berlin, Heidelberg, 1957), pp. 88–436. https://doi.org/10.1007/978-3-642-45869-9_2
4. N. Nakanishi, Prog. Theor. Phys. Suppl. **43**, 1 (1969). https://doi.org/10.1143/PTPS.43.1
5. P. Jain, H.J. Munczek, Phys. Rev. D **48**, 5403 (1993). https://doi.org/10.1103/PhysRevD.48.5403
6. H.J. Munczek, Phys. Rev. D **52**, 4736 (1995). https://doi.org/10.1103/PhysRevD.52.4736
7. P. Maris, P.C. Tandy, Phys. Rev. C **61**, 045202 (2000). https://doi.org/10.1103/PhysRevC.61.045202
8. I.C. Cloet, G. Eichmann, B. El-Bennich, T. Klahn, C.D. Roberts, Few Body Syst. **46**, 1 (2009). https://doi.org/10.1007/s00601-009-0015-x
9. B. El-Bennich, J.P.B.C. de Melo, B. Loiseau, J.P. Dedonder, T. Frederico, Braz. J. Phys. **38**, 465 (2008). https://doi.org/10.1590/S0103-97332008000400016
10. H. Sanchis-Alepuz, R. Williams, R. Alkofer, Phys. Rev. D **87**, 096015 (2013). https://doi.org/10.1103/PhysRevD.87.096015
11. E. Weil, G. Eichmann, C.S. Fischer, R. Williams, Phys. Rev. D **96**, 014021 (2017). https://doi.org/10.1103/PhysRevD.96.014021
12. G. Eichmann, C.S. Fischer, E. Weil, R. Williams, Phys. Lett. B **797**, 134855 (2019). https://doi.org/10.1016/j.physletb.2019.134855. [Erratum: Phys. Lett. B 799, 135029 (2019)]
13. G. Eichmann, C.S. Fischer, R. Williams, Phys. Rev. D **101**, 054015 (2020). https://doi.org/10.1103/PhysRevD.101.054015
14. A.S. Miramontes, H.S. Alepuz, R. Alkofer, Phys. Rev. D **103**, 116006 (2021). https://doi.org/10.1103/PhysRevD.103.116006
15. A. Miramontes, A. Bashir, K. Raya, P. Roig, Phys. Rev. D **105**, 074013 (2022). https://doi.org/10.1103/PhysRevD.105.074013
16. Y.-Z. Xu, M. Ding, K. Raya, C.D. Roberts, J. Rodríguez-Quintero, S.M. Schmidt, Eur. Phys. J. C **84**, 191 (2024). https://doi.org/10.1140/epjc/s10052-024-12518-x
17. G. Eichmann, C.S. Fischer, E. Weil, R. Williams, Phys. Lett. B **774**, 425 (2017). https://doi.org/10.1016/j.physletb.2017.10.002
18. K. Raya, L. Chang, A. Bashir, J.J. Cobos-Martinez, L.X. Gutiérrez-Guerrero, C.D. Roberts, P.C. Tandy, Phys. Rev. D **93**, 074017 (2016). https://doi.org/10.1103/PhysRevD.93.074017
19. Y.-Z. Xu, JHEP **07**, 118 (2024). https://doi.org/10.1007/JHEP07(2024)118
20. A.S. Miramontes, K. Raya, A. Bashir, P. Roig, G. Paredes-Torres, Chin. Phys. C **49**, 083108 (2025). https://doi.org/10.1088/1674-1137/add259
21. Y.-Z. Xu, A. Bashir, K. Raya, J. Rodríguez-Quintero, J. Segovia, Phys. Lett. B **869**, 139864 (2025). https://doi.org/10.1016/j.physletb.2025.139864
22. A.S. Miramontes, G. Eichmann, R. Alkofer, Phys. Lett. B **868**, 139659 (2025). https://doi.org/10.1016/j.physletb.2025.139659
23. G. Eichmann, H. Sanchis-Alepuz, R. Williams, R. Alkofer, C.S. Fischer, Prog. Part. Nucl. Phys. **91**, 1 (2016). https://doi.org/10.1016/j.ppnp.2016.07.001
24. P. Maris, P.C. Tandy, Phys. Rev. C **60**, 055214 (1999). https://doi.org/10.1103/PhysRevC.60.055214
25. R. Alkofer, P. Watson, H. Weigel, Phys. Rev. D **65**, 094026 (2002). https://doi.org/10.1103/PhysRevD.65.094026
26. D. Nicmorus, G. Eichmann, A. Krassnigg, R. Alkofer, Phys. Rev. D **80**, 054028 (2009). https://doi.org/10.1103/PhysRevD.80.054028

27. T. Hilger, M. Gomez-Rocha, A. Krassnigg, Phys. Rev. D **91**, 114004 (2015). https://doi.org/10.1103/PhysRevD.91.114004
28. T. Hilger, C. Popovici, M. Gomez-Rocha, A. Krassnigg, Phys. Rev. D **91**, 034013 (2015). https://doi.org/10.1103/PhysRevD.91.034013
29. F.F. Mojica, C.E. Vera, E. Rojas, B. El-Bennich, Phys. Rev. D **96**, 014012 (2017). https://doi.org/10.1103/PhysRevD.96.014012
30. F.E. Serna, B. El-Bennich, G. Krein, Phys. Rev. D **96**, 014013 (2017). https://doi.org/10.1103/PhysRevD.96.014013
31. Á.S. Miramontes, R. Alkofer, C.S. Fischer, H. Sanchis-Alepuz, Phys. Lett. B **833**, 137291 (2022). https://doi.org/10.1016/j.physletb.2022.137291
32. F. Gao, A.S. Miramontes, J. Papavassiliou, J.M. Pawlowski, Phys. Lett. B **863**, 139384 (2025). https://doi.org/10.1016/j.physletb.2025.139384
33. A.S. Miramontes, J.M.M. Chavez, J. Papavassiliou, J.M. Pawlowski, Eur. Phys. J. C **85**, 1055 (2025). https://doi.org/10.1140/epjc/s10052-025-14774-x
34. D. Brömmel et al. (QCDSF/UKQCD), Eur. Phys. J. C **51**, 335 (2007). https://doi.org/10.1140/epjc/s10052-007-0295-6
35. R. Frezzotti, V. Lubicz, S. Simula (ETM), Phys. Rev. D **79**, 074506 (2009). https://doi.org/10.1103/PhysRevD.79.074506
36. P.A. Boyle, J.M. Flynn, A. Juttner, C. Kelly, H.P. de Lima, C.M. Maynard, C.T. Sachrajda, J.M. Zanotti, JHEP **07**, 112 (2008). https://doi.org/10.1088/1126-6708/2008/07/112
37. S. Aoki et al. (JLQCD, TWQCD), Phys. Rev. D **80**, 034508 (2009). https://doi.org/10.1103/PhysRevD.80.034508
38. B.B. Brandt, A. Jüttner, H. Wittig, JHEP **11**, 034 (2013). https://doi.org/10.1007/JHEP11(2013)034
39. H.B. Meyer, Phys. Rev. Lett. **107**, 072002 (2011). https://doi.org/10.1103/PhysRevLett.107.072002
40. F. Erben, J.R. Green, D. Mohler, H. Wittig, Phys. Rev. D **101**, 054504 (2020). https://doi.org/10.1103/PhysRevD.101.054504
41. A. Accardi et al., Eur. Phys. J. A **60**, 173 (2024). https://doi.org/10.1140/epja/s10050-024-01282-x
42. R.A. Khalek et al., Nucl. Phys. A **1026**, 122447 (2022). https://doi.org/10.1016/j.nuclphysa.2022.122447
43. D.P. Anderle et al., Front. Phys. (Beijing) **16**, 64701 (2021). https://doi.org/10.1007/s11467-021-1062-0
44. G. Eichmann, R. Alkofer, I.C. Cloet, A. Krassnigg, C.D. Roberts, Phys. Rev. C **77**, 042202 (2008). https://doi.org/10.1103/PhysRevC.77.042202
45. S. Xu, X.-N. Li, X.-G. Wu, (2025b). arXiv:2507.07523 [hep-ph]
46. S.-X. Qin, L. Chang, Y.-X. Liu, C.D. Roberts, D.J. Wilson, Phys. Rev. C **84**, 042202 (2011). https://doi.org/10.1103/PhysRevC.84.042202
47. W. Jaus, Phys. Rev. D **41**, 3394 (1990). https://doi.org/10.1103/PhysRevD.41.3394
48. S.J. Brodsky, J.R. Hiller, Phys. Rev. D **46**, 2141 (1992). https://doi.org/10.1103/PhysRevD.46.2141
49. G. Eichmann, D. Nicmorus, Phys. Rev. D **85**, 093004 (2012). https://doi.org/10.1103/PhysRevD.85.093004
50. S. Zafeiropoulos, P. Boucaud, F. De Soto, J. Rodríguez-Quintero, J. Segovia, Phys. Rev. Lett. **122**, 162002 (2019). https://doi.org/10.1103/PhysRevLett.122.162002
51. W. Celmaster, R.J. Gonsalves, Phys. Rev. D **20**, 1420 (1979). https://doi.org/10.1103/PhysRevD.20.1420
52. A. Hasenfratz, P. Hasenfratz, Phys. Lett. B **93**, 165 (1980). https://doi.org/10.1016/0370-2693(80)90118-5
53. E. Braaten, J.P. Leveille, Phys. Rev. D **24**, 1369 (1981). https://doi.org/10.1103/PhysRevD.24.1369
54. A. Athenodorou, D. Binosi, P. Boucaud, F. De Soto, J. Papavassiliou, J. Rodriguez-Quintero, S. Zafeiropoulos, Phys. Lett. B **761**, 444 (2016). https://doi.org/10.1016/j.physletb.2016.08.065
55. C. Itzykson, J.B. Zuber, *Quantum Field Theory, International Series in Pure and Applied Physics* (McGraw-Hill, New York, 1980)
56. V.A. Miransky, *Dynamical Symmetry Breaking in Quantum Field Theories* (WORLD SCIENTIFIC, 1994). https://doi.org/10.1142/2170
57. M.R. Frank, Phys. Rev. C **51**, 987 (1995). https://doi.org/10.1103/PhysRevC.51.987
58. A.S. Miramontes, H. Sanchis-Alepuz, Eur. Phys. J. A **55**, 170 (2019). https://doi.org/10.1140/epja/i2019-12847-6
59. M. Leutnant, A. Sternbeck, PoS Confin. **2018**, 095 (2018). https://doi.org/10.22323/1.336.0095
60. C. Tang, F. Gao, Y.-X. Liu, Phys. Rev. D **100**, 056001 (2019). https://doi.org/10.1103/PhysRevD.100.056001
61. J.S. Ball, T.-W. Chiu, Phys. Rev. D **22**, 2550 (1980). https://doi.org/10.1103/PhysRevD.22.2550. [Erratum: Phys. Rev. D 23, 3085 (1981)]
62. G. Eichmann, Acta Phys. Polon. Supp. **7**, 597 (2014). https://doi.org/10.5506/APhysPolBSupp.7.597
63. R. Williams, Phys. Lett. B **798**, 134943 (2019). https://doi.org/10.1016/j.physletb.2019.134943
64. W.H. Press, B.P. Flannery, S.A. Teukolsky, W.T. Vetterling, *Numerical Recipes in FORTRAN 77: The Art of Scientific Computing*, 2nd edn. (Cambridge University Press, Cambridge, 1992) http://www.worldcat.org/isbn/052143064X
65. H. Sanchis-Alepuz, R. Williams, Comput. Phys. Commun. **232**, 1 (2018). https://doi.org/10.1016/j.cpc.2018.05.020
66. C.N. Brown, C.R. Canizares, W.E. Cooper, A.M. Eisner, G.J. Feldmann, C.A. Lichtenstein, L. Litt, W. Loceretz, V.B. Montana, F.M. Pipkin, Phys. Rev. D **8**, 92 (1973). https://doi.org/10.1103/PhysRevD.8.92
67. C.J. Bebek et al., Phys. Rev. D **9**, 1229 (1974). https://doi.org/10.1103/PhysRevD.9.1229
68. T. Horn et al. (Jefferson Lab F(pi)-2), Phys. Rev. Lett. **97**, 192001 (2006). https://doi.org/10.1103/PhysRevLett.97.192001
69. S.R. Amendolia et al. (NA7), Nucl. Phys. B **277**, 168 (1986). https://doi.org/10.1016/0550-3213(86)90437-2
70. E.B. Dally et al., Phys. Rev. Lett. **45**, 232 (1980). https://doi.org/10.1103/PhysRevLett.45.232
71. J. Volmer et al. (Jefferson Lab F(pi)), Phys. Rev. Lett. **86**, 1713 (2001). https://doi.org/10.1103/PhysRevLett.86.1713
72. R.J. Hernández-Pinto, L.X. Gutiérrez-Guerrero, A. Bashir, M.A. Bedolla, I.M. Higuera-Angulo, Phys. Rev. D **107**, 054002 (2023). https://doi.org/10.1103/PhysRevD.107.054002
73. B. Almeida-Zamora, J.J. Cobos-Martinez, A. Bashir, K. Raya, J. Rodríguez-Quintero, J. Segovia, Phys. Rev. D **109**, 014016 (2024). https://doi.org/10.1103/PhysRevD.109.014016
74. G. Wang, J. Liang, T. Draper, K.-F. Liu, Y.-B. Yang (chiQCD), Phys. Rev. D **104**, 074502 (2021). https://doi.org/10.1103/PhysRevD.104.074502
75. K.U. Can, G. Erkol, M. Oka, A. Ozpineci, T.T. Takahashi, Phys. Lett. B **719**, 103 (2013). https://doi.org/10.1016/j.physletb.2012.12.050
76. D. Stamen, D. Hariharan, M. Hoferichter, B. Kubis, P. Stoffer, Eur. Phys. J. C **82**, 432 (2022). https://doi.org/10.1140/epjc/s10052-022-10348-3
77. T.P. Leplumey, P. Stoffer, (2025). arXiv:2501.09643 [hep-ph]
78. R.L. Workman et al. (Particle Data Group), PTEP **2022**, 083C01 (2022). https://doi.org/10.1093/ptep/ptac097
79. G. Eichmann, (2025). arXiv:2503.10397 [hep-ph]
80. M.S. Bhagwat, P. Maris, Phys. Rev. C **77**, 025203 (2008). https://doi.org/10.1103/PhysRevC.77.025203
81. G. Eichmann, Hadron properties from QCD bound-state equations. Ph.D. thesis, Graz U. (2009)